



Full Text View

[Volume 29, Issue 10 \(October 1999\)](#)

Journal of Physical Oceanography

Article: pp. 2487–2503 | [Abstract](#) | [PDF \(533K\)](#)

Central Water Vortices of the Eastern North Atlantic

Jérôme Paillet

Service Hydrographique et Océanographique de la Marine, Centre Militaire d'Océanographie, Brest, France

(Manuscript received April 29, 1998, in final form October 26, 1998)

DOI: 10.1175/1520-0485(1999)029<2487:CWVOTE>2.0.CO;2

ABSTRACT

A set of 102 high-resolution hydrographic lines (mostly XBT lines) in the eastern North Atlantic is used to study baroclinic vortices dynamically intensified within the Central Water layer. First, for the sake of comparison with recent results from altimetry, spatial statistics of the main thermocline dynamic height are computed. The dynamic height wavenumber spectrum slope (close to k^{-3} at wavelengths shorter than 300 km), and the decrease with latitude of eddy scales deduced from its autocorrelation function, are found to be consistent with previous, local altimetric results.

Then, using a criterion of local temperature anomaly relative to the large-scale trend along each line, 162 Central Water mesoscale vortices are detected. Their distribution is heterogeneous, vortices of different size, sign, and intensity being found in most places. They have a mean apparent diameter (chord along the line) of 110 ± 50 km. It is estimated that a range of 100–145 Central Water vortices coexist at the same time between 20°N and 55°N , east of 34°W . Statistics of their location are consistent with previous observations suggesting that instability of the North Atlantic Current, of the Azores Current, and of the poleward eastern boundary current are the major formation processes for these vortices. The latter process is thought to account for the higher total number of anticyclones (87) than of cyclones (75), and for the eastward decrease of the mean vortex diameter. There is, on the other hand, no clear correlation between vortex size and latitude or local internal Rossby radius, contrarily to what scales of the general eddy variability show. Statistics of several other hydrological and dynamical properties of the vortices are briefly discussed. Finally, the eddy kinetic energy at 100-m depth associated with the field of vortices is crudely estimated, and found to amount to around half of the total observed eddy kinetic energy. These findings are compared with results from theory, models, and altimetry.

Table of Contents:

- [Introduction](#)
- [Data](#)
- [Properties of the 100–700-m](#)
- [Method for detecting](#)
- [Vortex statistics](#)
- [Discussion](#)
- [REFERENCES](#)
- [TABLES](#)
- [FIGURES](#)

Options:

- [Create Reference](#)
- [Email this Article](#)
- [Add to MyArchive](#)
- [Search AMS Glossary](#)

Search CrossRef for:

- [Articles Citing This Article](#)

Search Google Scholar for:

- [Jérôme Paillet](#)

1. Introduction

Many types of “eddy” (nonstationary) movements coexist in the eastern North Atlantic. An important family is that of mesoscale coherent structures associated with nearly symmetric and rotating circulation patterns, called “vortices” in this paper. Little is known about the part of the oceanic “eddy” variability and energy that can be attributed to vortices. However, vortices are of particular interest because, contrary to stable waves, for instance, they carry water parcels with them. Furthermore, vortices have their own displacement dynamics ([McWilliams and Flierl 1979](#)) and stability properties ([Hua 1988](#)). The mixing that they induce on a large scale is likely not to be isotropic or “Fickian,” and they may contribute to transport budgets as an advective term (see [Gent et al. 1995](#)).

During the last 25 years, the study of mesoscale variability in the North Atlantic has benefitted from many in situ observations. Local arrays of hydrology and current-meter moorings (MODE, LDE, TOURBILLON, SEMAPHORE), high-resolution hydrographic lines [POLYMODE, Warmwatersphere, World Ocean Circulation Experiment (WOCE), . . .], float tracking, and satellite measurements of sea surface temperature and height have been analyzed for that purpose. At the same time, studies have been carried out with increasingly sophisticated “eddy-resolving” models. From both approaches our knowledge of the North Atlantic eddy field has greatly improved, yet much remains to be learned about the eastern basin regime. In the western North Atlantic, mesoscale activity in the main thermocline is dominated by Gulf Stream instabilities, which produce the large and intense warm-core and cold-core rings [for a review see [Richardson \(1983\)](#)]. In the eastern North Atlantic, the situation seems more complex as there are many sources of eddies. The general circulation is now quite well known, dominated by the North Atlantic Current (NAC) that flows northeastward between 45°N and 55°N as multiple fronts, and the Azores Current (AC) that flows nearly zonally between 30°N and 35°N ([Sy 1988](#); [Paillet and Mercier 1997](#)). Instabilities of both currents were found to result in the shedding of cold-core cyclonic vortices to the south of their path (NAC: [Howe and Tait 1967](#); [Kupferman et al. 1986](#) and AC: [Gould 1985](#); [Tychensky et al. 1998](#)). Anticyclonic vortices with homogeneous cores have also been observed during the TOURBILLON experiment ([Le Groupe Tourbillon 1983](#)) and along high-resolution hydrographic lines (see, e.g., [Tsuchiya et al. 1992](#); [Arhan et al. 1994](#); [Pollard et al. 1996](#)). [Pingree and Le Cann \(1992\)](#) identified the instability of the poleward, eastern boundary slope current as a source of small anticyclones with such a homogeneous core, called “swoddies.” Farther down in the water column, anticyclonic lenses of Mediterranean Water have been shown to detach from the saline vein flowing poleward along the Iberian continental slope at around 1000-m depth ([Armi and Zenk 1984](#); [Bower et al. 1997](#)), and some of these “meddies” were shown to have a significant dynamical signature at the surface ([Stammer et al. 1991](#); [Schultz Tokos et al. 1994](#); [Tychensky and Carton 1998](#)). At around 2000-m depth, cyclonic lenses of deep Mediterranean Water ([Schauer 1989](#); [Colin de Verdière et al. 1989](#)) and anticyclonic lenses of Labrador Sea Water ([Paillet et al. 1998](#)) were also recently evidenced.

Statistical properties of the North Atlantic surface eddy field have been investigated using satellite measurements: [Le Traon et al. \(1990\)](#) and [Stammer and Böning \(1992\)](#) from Geosat altimeter data, and [Stammer and Böning \(1996\)](#) from TOPEX/Poseidon altimeters data, computed the eddy kinetic energy (EKE), wavenumber spectra of sea level anomaly, and corresponding eddy length scales. [Krauss et al. \(1990\)](#) estimated the latter quantities from infrared satellite images and from drifting buoy trajectories. All these authors conclude that there is a general decrease of eddy length scales with latitude, and also show that EKE is much lower in the eastern than in the western basin. Still, high-resolution numerical models with realistic bathymetry and simplified forcings show an EKE in the eastern basin that is too low by a factor of 2 to 10 ([Tréguier 1992](#); [Beckmann et al. 1994](#); [DYNAMO group 1997](#)). The deficiency is particularly strong in the mesoscale frequency band (periods of less than 150 days; see [Tréguier 1992](#); [Stammer et al. 1996](#)). One general interest of studying the eastern basin eddy field is to try to understand what processes are lacking in models of that area and what is needed to improve them.

Despite their likely importance in the total energy distribution, and in mixing and transport processes, mesoscale vortices intensified within the Central Water (CW) of the eastern North Atlantic are poorly known, contrary to Gulf Stream rings and meddies, for instance, whose strong hydrological signature notably allowed census of their distribution to be made ([Richardson 1983](#); [Richardson et al. 1991](#)). From satellite altimetry only a sea level anomaly (SLA) relative to an Eulerian time mean could be computed so far because of the lack of precision on the geoid at small scales. Eastern North Atlantic vortices cannot be firmly detected using the SLA, because a meander or a spatial shift of a strong current has the same signature as an isolated vortex. For the same reason, and also because they do not have very strong hydrological signature, it is not possible to detect CW vortices by only comparing a local data to a climatology. They also cannot be definitely detected by infrared imagery because of the rather high cloud coverage in the area and because many CW vortices do not have a surface thermal signature. Therefore, it is mostly by analyzing high-resolution hydrography or float tracks that some of them were discovered. [Gould \(1983\)](#) synthesized what was known about CW vortices in the early 1980s. Then, only five of them had been clearly identified and thoroughly sampled, but it was indicated that several more had been encountered during POLYMODE high-resolution XBT surveys, with “dimensions of the order of 100–200 km and isotherm displacements of order 100 m.”

The main goal of this work is to detect CW vortices using high-resolution XBT and CTD lines and analyze the statistics of their distribution and properties. Among the questions that will be addressed, are: Is there a cyclone–anticyclone asymmetry, as in some turbulence models (e.g., [Cushman Roisin and Tang 1990](#))? Is there a relation between the vortex size and the internal Rossby radius? Are vortices more numerous or more intense at some well-defined locations? What part of the near-

surface EKE can be attributed to this type of structure? It is also hoped that mapping CW vortices distribution and properties will help elucidate the processes of their formation and later evolution, and give insights into their role in transport processes such as thermocline ventilation. Finally, this study will provide a comparison basis for analyzing numerical model results and satellite measurements.

The dataset is described in [section 2](#), and for the sake of comparison with recent results from altimetry, spectral properties of the 100–700 m dynamic height are briefly analyzed in [section 3](#). The method for detecting CW vortices is presented in [section 4](#). [Section 5](#) examines the statistics of vortex distribution and properties. Finally the physical processes involved in the birth and life of CW vortices are discussed in [section 6](#).

2. Data

In order to find vortices in the mesoscale range (i.e., of typically 50–300 km diameter) that have a signature in the CW, hydrographic lines satisfying the following criteria have been looked for:

- near rectilinearity,
- near synopticity,
- total length of more than 400 km,
- mean horizontal resolution better than 30 n mi (56 km),
- measurements to at least 800-m depth in general,
- independence between lines.

First searching in the Service Hydrographique et Océanographique de la Marine (SHOM, French Navy Oceanographic Office) database, 73 such lines were found ([Fig. 1a](#)). All are measurements taken from French Navy ships between 1980 and 1996, mostly with Sippican T5 XBTs (measuring down to 2000 m), and for three lines with a mixture of T5 XBTs, XCTDs, and CTDs. Ten XBT lines were extracted from the Institut für Meteorologie (IFM) Kiel Warmwatersphere dataset of the 1980s (courtesy of M. Knoll), visible in the southern part of the map of [Fig. 1b](#). Three more XBT lines (rearranged into four) were finally extracted from the Tropical Ocean Global Atmosphere/WOCE Global Subsurface Data Center¹ of IFREMER/SISMER, and appear in the northern part of the map of [Fig. 1b](#). The data went through severe quality control procedures, and the expected precision on temperature is better than 0.1°C.

Fifteen recent high-resolution CTD lines were added to that dataset. These lines, shown in [Fig. 1c](#), match all the aforementioned criteria except that horizontal resolution is only requested to be better than 50 n mi (93 km). They were gathered between 1977 and 1989 [full description and references can be found in [Paillet et al. \(1998\)](#)], and provide accurate measurements of T and S down to the ocean bottom in most of the cases, which will prove helpful for dynamical calculations in [sections 3](#) and [5c](#).

General properties of XBT and CTD datasets are summarized in [Table 1](#). The mean station spacing of XBT lines, 26 km, is much better than the maximum requested (56 km), which ensures that vortices of more than 50-km diameter should be detected. On the other hand, structures of less than 100-km scale are not well sampled in the CTD lines. The whole dataset, shown in [Fig. 1d](#), is made up of more than 3400 profiles and covers quite well, although not regularly, the domain of study (20°–55°N, east of 40°W).

3. Properties of the 100–700-m dynamic height

Statistical properties of oceanic turbulence in the eastern North Atlantic have been mostly investigated through analyses of altimetric measurements. [Le Traon et al. \(1990\)](#) and [Stammer and Böning \(1992, 1996\)](#) find that the wavenumber spectrum of the SLA behaves like k^{-3} east of 40°W, for wavelengths smaller than a mesoscale spectral break at a few hundred kilometers. In the near Gulf Stream (more energetic) areas, steeper slopes of k^{-4} to k^{-5} are observed, consistent with quasigeostrophic turbulence theories ([Charney 1971](#); [Rhines 1979](#)) that predict in the wavenumber domain of enstrophy cascade a k^{-3} slope for the velocity spectrum, equivalent through geostrophy to a k^{-5} slope for the SLA spectrum. Eddy lengthscales deduced from the SLA autocovariance function are found to decrease with latitude and to increase quasi-linearly with the first internal Rossby radius. Before trying to detect CW vortices, these findings will be compared with statistical properties deduced from the present dataset. Apart from the natural interest of comparing two such different datasets, this will prove helpful for the interpretation of vortex properties in [section 6](#).

Neither the absolute sea level, nor the SLA relative to a local mean, can be computed from temperature profiles. The quantity deduced from hydrographic data that is closest to the absolute sea level is the dynamic height relative to a level where velocities are low. In the eastern North Atlantic, estimating salinity from temperature profiles is made difficult by the large $T-S$ scatter induced by the Mediterranean Water, and XBT data cannot be used to compute dynamic height relative to a deep level. Nevertheless, since a tight relation exists between T and S in the eastern North Atlantic Central Water, dynamic height relative to a shallow level can be computed from temperature profiles with satisfactory precision (Emery 1983). Figure 2 displays the $T-S$ scatterplot for the whole CTD dataset of Fig. 1c, between depth 100 and 700 m. Despite the saline “tail” at $10^\circ-11^\circ\text{C}$ due to a few stations that sample the upper MW vein or shallow meddies, a second degree polynomial fit $\hat{S}(T)$ to this data² explains 96% of the variance and yields a standard deviation of $(\hat{S} - S)$ of 0.08 psu. Dynamic height at 100 dbar relative to 700 dbar (H_{dyn} hereafter) is estimated as a function of $[T, \hat{S}(T), P]$ with an accuracy, estimated from CTD data, of 2 dyn cm. This is acceptable since absolute values of H_{dyn} in the basin range from 30 to 85 dyn cm (Stommel et al. 1978). Current meter data in the basin (Colin de Verdière et al. 1989; Müller and Siedler 1992) have shown that components of the flow along the barotropic and first baroclinic dynamical modes are highly correlated and altogether account for most of the energy of the fluid column so that *scales* of correlation and energy distribution of H_{dyn} should be similar to those of absolute sea level.

CTD-derived H_{dyn} and XBT-derived \hat{H}_{dyn} were linearly detrended along each line and interpolated at 5-km resolution. Assuming isotropy, the mean one-dimensional wavenumber spectra were then computed in two latitude bands, $20^\circ-40^\circ\text{N}$ and $40^\circ-55^\circ\text{N}$, by averaging individual spectra in the resolved wavenumber range (wavelength $\lambda > 130$ km for CTD lines, $\lambda > 50$ km for XBT lines). The resulting spectra are shown in Fig. 3. The assumption of isotropy could not be verified with the present, too sparse dataset, but no significant anisotropy has ever been evidenced in altimetric studies. In both latitude bands these spectra are characterized by a red energy drop for wavelengths around 1000 km, then by a white “plateau” down to a wavelength of about 300–400 km, and by another red drop with a slope of about k^{-3} down to 50-km wavelength. This shape is consistent with the aforementioned altimetry-deduced SLA spectra, except for the red part around $\lambda = 1000$ km. The peak at long wavelengths may be partly due to the energy of the *mean* circulation, whose effects are eliminated when estimating the sea level *anomaly*, but not fully removed when only detrending the data along each line. Anyway, the most notable result of the present analysis is that the spectral slope of sea level in the lower mesoscale band is close to k^{-3} in the eastern North Atlantic, and is thus less steep than in the western basin or than what quasigeostrophic theory predicts in the domain of enstrophy cascade. Stammer and Böning (1992) first thought that the weaker slopes of the eastern basin were due to noise in Geosat data, an argument which was refuted by Le Traon (1993). The recent spectra obtained with the less noisy TOPEX/Poseidon data (Stammer and Böning 1996, Fig. 6.9) also show near k^{-3} slopes east of 35°W . Note, finally, that the spectra of temperature at a given vertical level, and of the 100–700-m integrated thermal content (not shown), have the same shapes and slopes as those of H_{dyn} .

The station spacing of CTD lines being too coarse, spatial autocovariance functions $C(r)$ of the dynamic height were computed only from the XBT-derived \hat{H}_{dyn} , linearly detrended along each line. The normalized autocovariance functions and their statistical uncertainties are shown in Fig. 4 for the same latitude bands as above. In the northern box ($40^\circ-55^\circ\text{N}$) the function reaches its first zero crossing at $L_0 = 125 \pm 13$ km. In the southern box ($20^\circ-40^\circ\text{N}$) it does not present a negative lobe around 200 km but reaches its first minimum, close to zero, at $L_0 \sim 165 \pm 20$ km. This scale L_0 may not be fully representative of the typical “eddy scale” because the horizontal lag of the first zero crossing is sensitive to the way that the long wavelength signal (including the time mean) is removed, which is only grossly done in our case because of the variable length of the lines. An integral, more robust lengthscale (Le Traon et al. 1990, 1991) was therefore computed:

$$L_1 = \int_0^{L_0} C(r) dr.$$

Here L_1 decreases slightly from the southern box (68 ± 7 km) to the northern one (60 ± 5 km). The behaviors of both L_0 and L_1 are consistent with the results of Stammer and Böning (1996, their Fig. 6.11). On average the internal (first baroclinic) Rossby radius R_i varies, according to Emery et al. (1984), from 33 km in the southern box to 16 km in the northern box. While the linear relations between L and R_i proposed by Krauss et al. (1990) or Stammer and Böning (1992, 1996) cannot be properly tested with the present dataset, one may note that none of the lengthscales is directly proportional to R_i . This point will be discussed in more detail in section 6. Statistical properties of the hydrographic dataset having proven consistent with results from altimetry, it is now used to detect and study Central Water vortices.

4. Method for detecting Central Water intensified, mesoscale vortices

a. What is the signature of a CW vortex?

A quasigeostrophic, baroclinic vortex is characterized by horizontal density gradients. In an axisymmetric vortex, the thermal wind relation can be written:

$$f \frac{\partial u_\theta}{\partial z} = - \frac{g}{\rho_0} \frac{\partial \rho}{\partial r}, \quad (1)$$

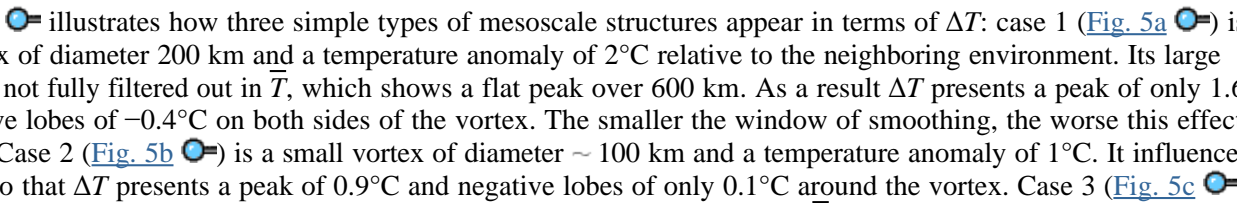

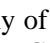
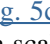
where f is the Coriolis parameter, $u_\theta(r, z)$ the azimuthal velocity, r the distance to the center, g the gravitational acceleration, and ρ the density. It implies that, within the baroclinic part of the vortex where the velocity shear is nonzero, density reaches an extremum at the center ($r = 0$) of the vortex. The maximum value of $|u_\theta(z)|$ is reached at the top of that layer of density anomaly. Attention is paid here to vortices *dynamically intensified* above 500-m depth, that are associated with a horizontal density extremum within the Central Water (above 700-m depth), and possibly below as well. In the eastern North Atlantic, CW-intensified cyclones are characterized by horizontal density maxima and temperature minima (cold vortices), and vice versa for anticyclones, these characteristics being detectable with XBT lines. The vertical displacement of isotherms has sometimes been used to characterize the eddy variability (e.g., [Dantzer 1977](#)), but in the eastern North Atlantic winter convection is also responsible for large isotherm displacements without strong horizontal gradients. The use of hydrographic lines allows one to work with horizontal temperature gradients, directly related to the velocity field by [\(1\)](#).

b. Decomposition of $T(x, z)$

In order to find and quantify temperature peaks at a constant $z = z_0$ along a line, temperature is decomposed into a low-passed component and a local (mesoscale) anomaly:

$$T(x, z_0) = \bar{T}(x, z_0) + \Delta T(x, z_0), (2)$$

x being the curvilinear abscissa along the line; $\bar{T}(x, z_0)$ is determined at each data point by a linear least squares fit on temperature at a constant depth over a 500-km window.³ Temperature anomaly ΔT is then deduced from [\(2\)](#).

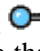
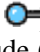
[Figure 5](#)  illustrates how three simple types of mesoscale structures appear in terms of ΔT : case 1 ([Fig. 5a](#) ) is a large vortex of diameter 200 km and a temperature anomaly of 2°C relative to the neighboring environment. Its large anomaly is not fully filtered out in \bar{T} , which shows a flat peak over 600 km. As a result ΔT presents a peak of only 1.6°C and negative lobes of -0.4°C on both sides of the vortex. The smaller the window of smoothing, the worse this effect would be. Case 2 ([Fig. 5b](#) ) is a small vortex of diameter ~ 100 km and a temperature anomaly of 1°C. It influences only slightly \bar{T} so that ΔT presents a peak of 0.9°C and negative lobes of only 0.1°C around the vortex. Case 3 ([Fig. 5c](#) ) is a sharp frontal zone of 2°C in 100 km, typical of the Azores Front or NAC fronts; \bar{T} follows the front, but on a scale of 600 km. As a consequence, ΔT presents two opposed lobes of 0.8°C amplitude that could be wrongly interpreted as two vortices. The larger the window of smoothing, the worse that effect would be. Cases 1 and 3 illustrate why a window of 500 km was chosen, after several tests, as a compromise. In the real ocean, identifying where a structure ends and what exactly is the environment is not possible. Decomposition [\(2\)](#) provides an imperfect but objective way to estimate the temperature anomaly of a structure. Some problems encountered with altimetric data are avoided here because \bar{T} is not a local time mean but a spatial mean at the time when the data was gathered. If a front is shifted relative to its time-mean position, the altimetric sea level shows anomalies at the current location as well as at the time-mean location because the front is “missing” there. Furthermore, both \bar{T} and ΔT will be used here, whereas with altimetry so far only the anomaly may be used.

c. Selection of CW vortices


It was decided that if $|\Delta T|$ exceeds 0.5°C over at least a 200-m vertical range between 100 and 700 m, the structure could be retained as a CW vortex (criterion A). With a vortex radius of 50 km, criterion A implies a minimum vertical shear of u_θ over the 200-m column of about 2.5 cm s⁻¹ [using [Eq. \(1\)](#) and $\hat{S}(T)$].

Then, neighboring profiles that present $|\Delta T| > 0.1^\circ\text{C}$, with ΔT of the same sign, over a 200-m vertical range are considered as being part of the same structure (criterion B). Because decomposition [\(2\)](#) tends to form lobes of opposite anomalies on both sides of a vortex, criterion B should efficiently reject profiles that are outside the vortex.

Applying criteria A and B, 248 possible CW vortices are identified, out of which some must be eliminated:

- Fifty-three are considered as artifacts of thermal fronts, as in the example of [Fig. 5c](#) , because there appears a neighboring pair of structures of opposite signs that shows a difference in \bar{T} of more than 1°C from one side to the other of the pair. Of these, 19 are thought to be artifacts of the NAC, 27 of the AC, and 7 of the Canary (or North Equatorial) Current.
- Five are likely to be meddies, having a signature strongly intensified below 600 m and vanishing above 400 m. [Pingree and Le Cann \(1993\)](#) describe a “shallow meddy” that has such a signature.
- Nineteen are considered as secondary poles of multipolar structures, or artifacts of a neighboring strong vortex (as in [Fig. 5a](#) ). On the other hand, when two neighboring vortices of opposite sign have comparable size and ΔT amplitude (dipole), both are retained.
- A vortex detected on only one expandable probe profile could be an artifact of a measurement error. Such a vortex is kept when at depths greater than 1500 m, its temperature reasonably matches that of neighboring profiles. Nine vortices detected with only one XBT were rejected because the profile did not reach these depths. Systematic errors in the fall rates of different expandable probes have been evidenced in the past (see, e.g., [Boyd and Linzell 1993](#)). These errors do not exceed a few tens of meters in the first 700 m, which should not alter the results of vortex detection. Anyway, in the few cases where a mixture of different types of probes were used, only vortices detectable on several consecutive profiles were found.

Finally 162 structures are kept, 87 anticyclones and 75 cyclones that will be described in [section 5](#). Some of these structures may well be meanders of a front, rather than detached vortices, if lines have cut meanders while running parallel to the axis of the front. This may particularly be the case in the NAC area where several lines are quasi zonal. The distinction is, anyway, hard to make between a well-formed mesoscale meander and a detached vortex. Although this is probably minor considering the existant literature, some of the selected vortices may also be artifacts of the internal wave field.


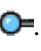
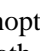
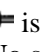
[Figure 6](#)  illustrates the selection process along an XBT line gathered by the French Navy Ship S/M *Le Bihan* along 12° 30'W in December 1994. Three structures satisfy criterion A: an anticyclone around 35°50'N is retained as a CW vortex; a cyclone–anticyclone pair between 33°20'N and 34°10'N is rejected for being a likely artifact of the Azores Front. Finally two other structures appear that do not satisfy criterion A: a possible cyclone around 37°30'N has a maximum $|\Delta T|$ of 0.9°C but not on sufficient vertical range. A meddy at 32°40'N presents maximum $|\Delta T|$ of over 2.0°C but only below 700-m depth.

d. Estimation of the vortex diameter

Criterion B defines which profiles are considered to be within a given vortex. Determining the vortex diameter, however, is not straightforward: the hydrographic line does not necessarily cross the vortex center, and the structure is likely to be elliptic rather than circular. Furthermore, the diameter defined by the water mass trapped into the vortex is not similar to its width of near solid-body rotation nor to its width of dynamical influence. Therefore, only the *chord* estimated along the line or “apparent” diameter D_a was computed, as follows: D_a is the sum of the distance between the two extreme data points inside the vortex, and half the distances between each of these points and the next one outside the vortex. Note that, if a vortex was circular, the mean chord estimated along lines crossing it at a random distance from the center would be the ratio of its surface to its diameter, or $(\pi/4) \times D_{\text{real}}$ ($\sim 0.8D_{\text{real}}$). On the other hand, a line crossing a vortex far from its center might not allow its detection with criterion A, so that the average underestimate on the diameter estimate is certainly less than 20%. Errors on the diameter estimation due to discrete sampling have been tested in simple cases. They differ for each vortex and do not seem to result in a systematic bias. The “real” vortex diameter associated with the water mass anomaly defined by criterion B is thus, for each vortex, most likely between $1.0D_a$ and $1.2D_a$.

5. Vortex statistics

a. General properties

The selected anticyclones are presented in [Fig. 7a](#) , and cyclones in [Fig. 7b](#) . Their size on the map is proportional to their apparent diameter D_a so that northern and southern vortices may be directly compared. The CW vortex distribution in [Fig. 7](#)  is influenced by the irregular distribution of the data, so these maps should not be thought of as synoptic, nor as mean situations. The most notable feature in [Fig. 7](#)  is the diversity of the vortex distribution: vortices of both signs and various size are found in most well-sampled places. No significant difference stands out at first sight between anticyclone and cyclone distributions. Of a total of 162 CW vortices, 18 are dynamically intensified below 100-m depth (11 anticyclones, 7 cyclones), presenting a ΔT at 100-m depth opposed to the vortex general temperature anomaly.

Two views are proposed to evidence large-scale trends in the set of CW vortices: A “pilot chart” (Fig. 8) presents the total number of selected cyclones and anticyclones with their mean D_a , the probability of vortex encounter, and the total expected number of coexisting vortices (see below) computed in geographic boxes containing at least 9000 km of hydrographic line. This figure is complemented by plots of several parameters against latitude and longitude, shown in Fig. 9.

The probability of vortex encounter P_V defined as the average number of vortices (or vortexlike meanders) found per kilometer of line shows well-defined trends clearly related with the mean circulation of the basin: the highest probabilities are found along the NAC path with values above $2.5 \times 10^{-3} \text{ km}^{-1}$ (or 2.5 vortices every 1000 km) north of 45°N , and along the AC path with values above $1.3 \times 10^{-3} \text{ km}^{-1}$ ($30^\circ\text{--}35^\circ\text{N}$ band, Fig. 9a; boxes 5 and 6, Fig. 8). The zonal evolution of P_V (Fig. 9b) reflects an eastward decrease of the total vortex probability due to the decrease of the cyclone probability, while the anticyclone probability remains nearly constant. The dominance of anticyclones (87 against 75) for the whole dataset is thus not regularly distributed: there are more cyclones than anticyclones in the west, and vice versa in the east (Fig. 9b), and it might be that more anticyclones are found as a total just because there is more data in the eastern than in the western part of the domain (Fig. 1d). Regional variations of the parity bias are discussed in section 6 below. The local probability for being into a vortex is approximately given by $P_V \cdot \bar{D}_a$ (D_a quantifying the length of hydrographic line inside a vortex, after criterion B). This number multiplied by the ratio of the total surface of a box to the mean surface of a vortex estimates the total number N_V of vortices that coexist at the same time in a box, displayed in Fig. 8. With D_{real} belonging to $(D_a, 1.2D_a)$, a range of 100–145 CW vortices are found to exist at the same time in the domain of Fig. 8 (east of 34°W). The number of coexisting CW vortices in boxes 5, 6, and 7 amounts to 42–61, which the reader may compare to the estimate by Richardson et al. (1991) of 24 coexisting meddies in approximately the same domain.

The vortex size D_a does not present a marked decrease with latitude (Fig. 9c), as one would expect from the evolution of eddy length scales discussed in section 3. The correlation between D_a and the local internal Rossby radius R_i given by Emery et al. (1984) is only of 0.04. A least squares fit between D_a and latitude yields an insignificant decrease of the mean D_a (112 km against 109 km) between 30°N and 50°N , while R_i decreases by more than a factor 2. There is, on the other hand, a significant decrease of D_a with longitude (Figs. 8 and 9d), for vortices of both sign. A least squares fit yields a decrease from $D_a \sim 121 \text{ km}$ at 30°W to $D_a \sim 93 \text{ km}$ at 10°W . Tentative explanations for these characteristics are given in section 6. The standard deviations on the box averaging of Figs. 9c,d are quite large ($\sim 40 \text{ km}$), confirming the heterogeneity of the vortex distribution.

Figures 9e,f show the zonal and meridional evolution of the mean absolute temperature anomaly $|\overline{\Delta T}|$ at the center of CW vortices. $\overline{\Delta T}$ is representative of the baroclinic “momentum” of a vortex: on an f plane, the thermal wind equation (1) implies that it is at first order proportional to $\int u_\theta dr$, with u_θ being the azimuthal geostrophic velocity at 100 m relative to 700 m. The main difference between cyclone and anticyclone statistics is found between 40° and 50°N , west of 30°W where the mean $|\overline{\Delta T}|$ of cyclones is much higher than that of anticyclones. This is mostly due to the presence of two very intense ($\overline{\Delta T} < -3.5^\circ\text{C}$) cold core cyclones near 44°N , 36°W and 48°N , 38°W along a CTD line. If those two are left apart, the statistics would show for both types of vortex a weak increase of $\overline{\Delta T}$ toward the north (Fig. 9e) and an increase by a factor 2 toward the west (Fig. 9f). This evolution can be attributed to the presence of the NAC in the northwest of the domain. NAC instability gives birth to vortices that retain the strong thermal contrast of its fronts, and the two strongest cyclones are most probably cold core rings of the NAC born in the west of the domain where NAC temperature gradients are highest. Quite surprisingly, the numerous vortices found in the vicinity of the AC ($30^\circ\text{--}35^\circ\text{N}$, Fig. 9a) do not present a higher temperature anomaly than their neighbors, despite the fact that the AC is associated with a thermal front of 1°C to 2°C basinwide. Note, finally, that only a very weak correlation between vortex size D_a and intensity $\overline{\Delta T}$ has been found.

b. Mode water vortices and ventilation

Thermocline ventilation is the process by which the ocean acquires its thermohaline properties through exchanges with the atmosphere in the surface mixed layer, and by which these properties are transferred (“subducted”) into the interior, stratified and adiabatic ocean. Paillet and Mercier (1997) show that subduction rates are dominated in the area between the AC and the NAC by the formation and subduction of the light (temperature between 10.5°C to 12.5°C) variety of subpolar mode water (SPMW, McCartney and Talley 1982). Paillet and Arhan (1996) depict how this weakly stratified water is found in two distinct regimes: North of a line located around $40^\circ\text{--}42^\circ\text{N}$, it is sensitive to winter convection and found at the end of winter in the 0–500-m range. South of that line, it is clearly isolated from the atmospheric contact by a permanent “secondary pycnocline” around 200-m depth, and is found in the range 300–500 m. Paillet and Mercier (1997) find that the

weak southward flow in that region is associated with a relatively strong subduction transport ($2.5 \pm 0.4 \times 10^6 \text{ m}^3 \text{ s}^{-1}$) across that line. These studies suggest that ventilation in that area involves the large-scale dynamics of the mean ocean; however, mesoscale processes such as the transport of fluid into vortices from the north to the south of the subduction line could participate in the total subduction transport there.

A mode water is weakly stratified compared to the neighboring fluid because of its convective origin. Here a CW vortex is defined as containing SPMW if the vertical temperature gradient in its core is below $0.5^\circ\text{C}/100 \text{ m}$ over a 200-m vertical range, in the 200–500 m layer. [Figure 10](#) displays how these vortices are distributed with latitude. No SPMW vortex is found south of 35°N . North of 40°N , 35 SPMW anticyclones and 17 cyclones are found, respectively, 67% and 39% of the total number of each type there. Anticyclones are thus favorable sites for the mode water, which is consistent with their negative potential vorticity anomaly. Numerous such anticyclones with homogeneous cores have been observed in the region by [Arhan et al. \(1994\)](#) and [Pingree and Le Cann \(1992\)](#) notably. Finally, only three cyclones, and no anticyclone, contain SPMW between 35°N and 40°N . This implies that only little SPMW belongs to CW vortices south of the subduction line.

If one SPMW vortex crosses the subduction line each year, with an average radius of 50 km and subducting SPMW in the depth range 200–500 m, the process would contribute to subduction transport by $0.07 \times 10^6 \text{ m}^3 \text{ s}^{-1}$. A few vortices crossing the line each year would contribute to a small but nonnegligible transport. But, since quasigeostrophic cyclones tend to move naturally to the west-northwest in a fluid at rest ([McWilliams and Flierl 1979](#)), it is likely that the southward transport in cyclones is *due* to the mean southward advection, rather than *reinforcing* it. That no mode water anticyclone is found south of the subduction line also suggests that large-scale, advective dynamics seem appropriate to describe the ventilation regime in the area. It is nonetheless possible that vortices containing mode water mix quickly with the surroundings after having crossed the subduction line, and thus may not be detected in the present dataset, while playing a role in ventilation.

c. Dynamical properties

Although they are of much importance for modelers, vortex dynamical properties cannot be estimated precisely from our dataset. Relative geostrophic velocities can be computed from XBT-derived \hat{H}_{dyn} , but errors become too large in such a calculation that involves spatial derivation of H_{dyn} . Velocities can be estimated with a better precision from CTD data, but the relatively coarse CTD sampling may not allow one to infer details of the velocity structure. The purpose of this subsection is mainly to get an idea of the order of magnitude of the CW vortex azimuthal velocities and sea level anomalies, and check if there are significant differences between cyclones and anticyclones.

The geostrophic velocity component at 100-m depth normal to the line, u_{\perp} , is estimated from CTD lines by integrating vertically from 3000 m to 100 m the thermal wind relation projected along the line. Velocity relative to the center is estimated as $u'_{\perp} = u_{\perp} - \bar{u}_{\perp}$ (\bar{u}_{\perp} being averaged over all pairs of profiles inside or at the boundary of the vortex), and the absolute value of vorticity as $|\zeta| = 2[u'_{\perp\text{max}} - u'_{\perp\text{min}}]/\Delta x$, where Δx is the distance between the points where those maximal and minimal (maximum negative) velocities are found. The Rossby number is given as $\text{Ro} = |\zeta|/f$, and the geopotential anomaly at 100 m, expressed in meters, is

$$\eta = \int \frac{fu'_{\perp}}{g} dx.$$

These parameters may be significantly underestimated because of the poor measurement resolution and the eventual remoteness between the line and the center. [Table 2](#) summarizes the mean and rms values of $|u'_{\perp\text{max}}|$, ζ , Ro , and η_{max} for the whole sets of cyclones and anticyclones detected on CTD lines. They are smaller by 10%–25% for anticyclones than for cyclones, but this is mostly due to the influence of the two very strong NAC cold core rings mentioned in [section 5a](#). With $|u'_{\perp\text{max}}|$ around 20 cm s^{-1} , CW vortices are clearly nonnegligible features since mean currents are less than 10 cm s^{-1} in most of the basin. The less intense CW vortex has $|u'_{\perp\text{max}}|$ above 7 cm s^{-1} . Rossby numbers range between 0.02 and 0.17, which is small compared to one. This indicates that at the sampling scale, centrifugal effects are small and geostrophy is a good approximation of their dynamics, but it does not exclude that these vortices may have small ageostrophic cores. The sea level anomaly associated with a vortex is a quantity comparable to the geopotential anomaly η_{max} . Absolute values of η_{max} range between 2 and 40 cm, while the mean is around 13 cm. Most CW vortices could thus be detected by satellite altimetry, which now can be as precise as 2–3 cm, if the geoid was perfectly known.

Since only 48 CW vortices are detected in the CTD lines (26 anticyclones, 22 cyclones), large-scale geographic trends of the dynamic parameters are not very robust and are not displayed here, but in general the distributions of Ro and $|\eta_{\max}|$ are consistent with that of the temperature anomaly shown in [Figs. 9e,f](#), with maximum values in the NAC area.

d. Eddy kinetic energy

Subinertial eddy kinetic energy is the most standard quantity for comparing the level of turbulence in data and numerical ocean models. In the eastern North Atlantic, high-resolution models (up to $1/6^\circ$) fail to reproduce observed EKE levels (e.g., [Beckmann et al. 1994](#); [DYNAMO Group 1997](#)), although their mean currents have become quite realistic. [Stammer et al. \(1996\)](#) show that the deficiency is particularly strong at high frequency and wavenumber (periods below 100 days, wavelengths below 1000 km), which are those associated with mesoscale vortices. Current meter data analyses in the basin ([Gould 1983](#); [Mercier and Colin de Verdière 1985](#); [Müller and Siedler 1992](#)) show that a large amount (typically half) of the upper-ocean EKE takes place around 100 days period and less, but the part of that energy due to mesoscale vortices is unknown. This section aims at estimating the amount of EKE associated with CW vortices only (called VKE, for vortex kinetic energy, hereafter), which should give information on whether a good representation of these eddies in models is needed, and would be sufficient, to model a realistic EKE.

In a similar way as with altimetric data, assuming geostrophy and isotropy, VKE can be estimated from hydrography-derived velocities as

$$VKE = \frac{1}{\Delta L_{\text{tot}}} \int_{\text{lines}} u_{\perp}'^2 ds$$

with ΔL_{tot} being the total length of the hydrographic lines in a predefined area, and the velocities u_{\perp} being set to zero outside vortices.

As argued in [section 5c](#), u_{\perp}' can be precisely estimated only from CTD data, whose coverage is not sufficient to evidence regional variations of VKE. To make use of XBT data, the near proportionality between $\int u_{\theta} dr$ and $\int \Delta T dz$ due to the thermal wind relation [\(1\)](#) may be exploited. The latter term is measured by XBTs, while in a vortex in solid body rotation, the former term is proportional to VKE calculated over a vortex diameter. A linear fit (not shown) between

$$T_i = \int_{-700\text{m}}^{-100\text{m}} \Delta T dz \quad \text{and} \quad E_1 = \frac{1}{2R} \int_{-R}^R \frac{1}{2} (u_{\perp}'^2) dx,$$

both calculated for vortices detected in CTD data, explains 80% of the variance and gives a relation that may crudely be used to estimate E_1 from XBT data. VKE is obtained in regional boxes by summing up $E_1(T_i)$ for XBT vortices, E_1 directly computed for CTD vortices, and weighting the sum by the ratio of “inside vortices” to “total” line lengths. [Figure 11](#) presents the meridional evolution of VKE in two longitude bands (20° – 40°W and 0° – 20°W). An error bar on VKE is hard to estimate, but is likely to be larger than 20% because of data sparsity and of the many assumptions in the calculation. The meridional evolution of VKE in the 20° – 40°W band resembles that of CW vortex probability ([Fig. 9a](#)), with peaks in the AC and the NAC areas, and is reminiscent of EKE distributions obtained along 30°W by [Brügge \(1995\)](#) at 100-m depth from floats, and by [Stammer and Böning \(1996\)](#) from altimetry (both displayed in [Fig. 11](#)). VKE values range between one-fourth, in the low energy areas, and nearly all, in the NAC peak, of the total EKE observed by these authors. In the latter area (45° – 50°N band), the higher ratio of VKE to observed EKE can be due to the fact that several meanders of the NAC may have been taken for vortices (as discussed in [section 4](#)), so an unknown part of the mesoscale energy may be wrongly interpreted as being associated with vortices. In the 0° – 20°W band ([Fig. 11](#)), E_0 is significantly lower than in the 20° – 40°W band, by a factor of about 4, except between 35° and 40°N where both estimates are similar. This is consistent with the strong eastward decrease found with altimetric data at AC and NAC latitudes and with the eastward decrease of both vortex probability ([Fig. 9b](#)) and vortex intensity ([Fig. 9f](#)).

6. Discussion

a. Summary and general remarks

A total of 102 hydrographic lines, sampling 109 000 km in the eastern North Atlantic, have been analyzed. The wavenumber spectrum of dynamic height, and eddy scales deduced from its autocovariance function, are consistent with

earlier estimates of these quantities from altimetric data. While this does not prove these results to be true, it provides a “ground truth” confirmation of altimetric results and suggests that the present hydrographic data is sufficient to infer general statistical properties of the basin.


Using a criterion of alongline temperature anomaly, 162 CW-intensified mesoscale vortices have been detected and analyzed. Some of these CW vortices may not be isolated, long-living structures: if a line cuts the meander of a jet, while being parallel to the main jet axis, the structure is seen as a detached vortex. On the other hand, some real mesoscale, isolated structures that have a surface dynamical signature are not detected by the method. For instance, the subsurface-intensified anticyclone of the TOURBILLON experiment ([Le Groupe Tourbillon 1983](#)) near 47°N–15°W, has too weak a temperature anomaly within the CW layer to satisfy the selection criterion, its baroclinic shear being largest near 1000 m. It was decided, however, not to consider temperature anomalies below 700-m depth because they are often associated with meddies. The CW vortices detected here have a mean temperature anomaly over the layer 100–700 m of $0.8 \pm 0.5^\circ\text{C}$, and present a significant baroclinic shear above 700-m depth. They are quite intense mesoscale features, and their large number allows one to study statistics of their distributions and properties. These statistics show the following.

- On average 1.5 vortices are found every 1000 km of hydrographic line, yielding that 100–145 CW vortices should coexist at the same time in the domain. They have a mean apparent diameter of 110 ± 50 km, real diameters being likely to range between D_a and $1.2D_a$.
- There is no clear correlation between vortex diameter and latitude or local internal Rossby radius.
- Anticyclones are significantly more numerous than cyclones in the eastern part of the basin, while cyclones dominate in the western part. A few cyclones (here, two) are far more intense than other vortices, while statistical properties of the other vortices are very similar for cyclones and anticyclones.
- Few vortices containing subpolar mode water are found away from its area of formation, which suggests that advection of mode water trapped into vortices probably does not contribute to an important part of the subduction budget of the basin.
- Despite a lack of precision in the determination of vortex kinetic energy, these results suggest that CW vortices contribute to at least one-fourth, and generally around one-half, of the near-surface EKE in the basin and thus to a major part of the energy at periods between 5 and 100 days. Numerical models so far are almost devoid of mesoscale vortices in that basin. Classical explanations involve their lack of resolution and their excessive viscosity (e.g., [Treguier 1992](#)). To correctly reproduce the observed amount of EKE, models need to be able to form CW vortices and not dissipate them too fast, and therefore a very high resolution and low viscosity even at mid and low latitudes is needed.

One may think of altimetry as providing a better dataset for studying near-surface vortices. However, uncertainties in the geoid at scales of a few tens of kilometers make it hard to be sure that a local anomaly is indeed a vortex. Furthermore, altimetry cannot provide information on the thermal (and baroclinic) structure of a vortex and cannot distinguish between a CW vortex and a subthermocline vortex that has a surface signature. Therefore, analyses of high-resolution hydrographic lines remains a useful tool, complementary to altimetry, to study the mesoscale oceanic field.

We now discuss a few specific questions that the study results raise.

b. Why is the H_{dyn} spectrum slope less steep than k^{-5} ?

It is shown in [section 3](#) that the slope of H_{dyn} wavenumber spectrum in the eastern North Atlantic is about k^{-3} , less steep than in the western North Atlantic and than what quasigeostrophic turbulence theory and models predict in the domain of enstrophy cascade. These theories and models generally assume that there is an energy input to the system at some defined wavelength (typically, through baroclinic instability), then enstrophy cascade takes place at smaller wavelengths. This may be the situation in the western North Atlantic, where the production of large (~ 250 km diameter or half-wavelength) Gulf Stream rings dominates other near-surface mesoscale processes so that the spectral domain below 400-km wavelength may be dominated by enstrophy cascade. In the eastern North Atlantic, smaller vortices are produced and some with diameters below 80 km are found at every latitude ([Fig. 9c](#) ) so that the enstrophy cascade domain, if existent, would be less than 150-km wavelength. Neither altimetric nor hydrographic data so far have enough resolution to firmly measure that. The eastern North Atlantic in the spectral band between 150 and 500 km is likely to be characterized by a mixture of downscale enstrophy and upscale energy cascades, and by energy inputs in the whole band, that result in the observed k^{-3} spectral slope for the SLA.

c. Why is there no decrease of the vortex diameter with latitude?


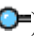

We saw in [section 3](#) that eddy scales (especially L_0) decrease with latitude and increase with the first internal Rossby radius R_i . Theory (e.g., [Gill 1982](#), pp. 557–561) states that the wavelength of the most unstable perturbation, in simple models of baroclinic instability, is proportional (with a factor near 2π) to R_i . Therefore, several authors ([Krauss et al. 1990](#); [Stammer and Böning 1992, 1996](#)) have suggested that baroclinic instability is the dominant process by which mesoscale perturbations appear in the North Atlantic. On the other hand, as noted by [Le Traon \(1993\)](#), neither L_0 nor L_1 show a true proportionality with R_i in the aforementioned studies, but rather a linear relation with some significant value at the origin. Thus, linear theory statements are not exactly fulfilled.


The strongest eddy-scale decrease with latitude is shown by scale L_0 , which is known to be quite sensitive to the way the mean signal and the noise are removed. The integral of the normalized autocorrelation function L_1 is more robust because the autocorrelation values at all lags between 0 and L_0 are taken into account. Both from altimetry and the present hydrographic data, L_1 is found to decrease only slightly with latitude, in a way more consistent with the evolution of the CW vortex diameter. It thus seems that scale L_0 is not truly representative of oceanic structures size. Since VKE is only a fraction of the total EKE ([section 5](#)), forms of eddy movements other than vortices may account for the difference of meridional behavior between vortex diameter and typical eddy scales, provided that this difference is statistically significant. A westward increase of the vortex radius has also been evidenced here, which may explain the large difference in eddy scales observed by [Mercier and Colin de Verdière \(1985\)](#) between western Atlantic MODE eastern Atlantic TOURBILLON areas.

That L_0 and L_1 do not show a true proportionality with R_i and that CW vortex diameters seem almost uncorrelated with R_i does not mean that baroclinic instability plays no role in the birth of mesoscale turbulence: First, the most unstable perturbation is not necessarily the one that is excited and grows in the real ocean. Second, even if, in the area of vortex formation, their diameters were proportional to R_i , this proportionality would not remain valid as vortices move away from their formation region. This is particularly the case when vortices grow on the continental slope (in relatively shallow depth and small R_i) to later be shed into the deep ocean. Third, vortices are known to coalesce with neighbors, this process being potentially most active where they are numerous. By this process, vortex diameter grows. In our particular case, since CW vortices are most numerous in the NAC area, coalescence may result in a stronger growth in the northern part of the domain than in the south, biasing the eventual relation between D_a and R_i at the time of vortex birth.

d. What do we learn about CW vortex formation processes?

Three known formation processes are identified in the introduction: the instabilities of the NAC, of the AC, and of the poleward eastern boundary current [that occurs most often in winter and gives birth to relatively small anticyclones; see [Pingree and Le Cann \(1990, 1991, 1993\)](#)]. The role of fluctuating wind forcing ([Frankignoul and Müller 1979](#)) has been invoked as a nonnegligible source of EKE at scales much larger than that of the CW vortices. Rough topography ([Treguier and Hua 1988](#)) may further transfer some of this energy to smaller scales.

The present dataset does not provide evidence of other generation mechanisms. Central Water vortices are more numerous in the vicinity of the NAC and AC, consistent with the likely role of their instabilities. Instability of the poleward eastern boundary current is most probably responsible for the presence of many small anticyclones near the eastern boundary ([Fig. 7a](#) ). This process can account for the eastward decrease of anticyclone diameter ([Fig. 9d](#) ) and the parity bias toward more anticyclones than cyclones in the eastern part of the basin ([Fig. 9b](#) ). About 25 such small anticyclones, found east of 20°W, are possible swoddies. This accounts for more than the anticyclone – cyclone difference in the whole dataset, 87 versus 75. Although some studies (e.g., Cushman Roisin and Tang 1989; [Polvani et al. 1994](#)) have shown a natural parity bias toward anticyclones in idealized models of decaying turbulence, in the case of the eastern North Atlantic the bias seems mostly due to the asymmetry of one of the formation process.

In the case of the Gulf Stream, instability creates a clear regional parity bias, with cyclonic cold core rings southeast and anticyclonic warm core rings northwest of its path. A similar tendency could be expected in the AC and NAC areas, but the present data show little evidence for that. In [Fig. 9a](#) , one may note that there are more cyclones than anticyclones south of the AC (20°–30°N band) and vice versa north of it (35°–40°N band). There are also a few more cyclones than anticyclones in the 40°–47°N band, west of 20°W, which is south of the average NAC path. These differences are small in comparison to the western North Atlantic regime. One conclusion is that there are anticyclones being formed south of the NAC and AC, and cyclones north of these currents. The detachment of a recirculation cell from the main current, or the formation of dipoles rather than monopoles during baroclinic instability, could give birth to such vortices.

Acknowledgments

I wish to thank Michaela Knoll for the IFM Kiel XBT data, and Philippe Delmee and Rolande Tournier for early work on the SHOM database. Fruitful discussions with several colleagues in Brest, and valuable comments by the two anonymous reviewers, are also acknowledged. This study is a contribution to the ARCANE program for which the most recent SHOM XRT lines were gathered.

REFERENCES

- Arhan, M., A. Colin de Verdière, and L. Mémerly, 1994: The eastern boundary of the subtropical North Atlantic. *J. Phys. Oceanogr.*, **24**, 1295–1316.. [Find this article online](#)
- Armi, L., and W. Zenk, 1984: Large lenses of highly saline Mediterranean Water. *J. Phys. Oceanogr.*, **14**, 1560–1576.. [Find this article online](#)
- Beckmann, A., C. W. Böning, C. Köberle, and J. Willebrand, 1994: Effects of increased horizontal resolution in a simulation of the North Atlantic Ocean. *J. Phys. Oceanogr.*, **24**, 326–344.. [Find this article online](#)
- Bower, A. S., L. Armi, and I. Ambar, 1997: Lagrangian observations of meddy formation during a Mediterranean undercurrent seeding experiment. *J. Phys. Oceanogr.*, **27**, 2545–2574.. [Find this article online](#)
- Boyd, J. D., and R. S. Linzell, 1993: The temperature and depth accuracy of Sippican T-5 XBTs. *J. Atmos. Oceanic Technol.*, **10**, 128–136.
- Brügge, B., 1995: Near-surface mean circulation and kinetic energy in the central North Atlantic from drifter data. *J. Geophys. Res.*, **100**, 20 543–20 554..
- Charney, J. G., 1971: Geostrophic turbulence. *J. Atmos. Sci.*, **28**, 1087–1095.. [Find this article online](#)
- Colin de Verdière, A., H. Mercier, and M. Arhan, 1989: Mesoscale variability transition from the western to the eastern Atlantic along 48° N. *J. Phys. Oceanogr.*, **19**, 1149–1170.. [Find this article online](#)
- Cushman Roisin, B., and B. Tang, 1990: Geostrophic turbulence and emergence of eddies beyond the radius of deformation. *J. Phys. Oceanogr.*, **20**, 97–113.. [Find this article online](#)
- Dantzer, H. L., Jr., 1977: Potential energy maxima in the tropical and subtropical North Atlantic. *J. Phys. Oceanogr.*, **7**, 512–519.. [Find this article online](#)
- DYNAMO Group, 1997: DYNAMO—Dynamics of North Atlantic Models: Simulation and assimilation with high resolution models. Berichte aus dem Institut für Meereskunde No. 294, Christian-Albrechts Universität, Kiel, Germany, 333 pp..
- Emery, W. J., 1983: On the geographical variability of the upper level mean and eddy fields in the North Atlantic and North Pacific. *J. Phys. Oceanogr.*, **13**, 269–291.. [Find this article online](#)
- , W. G. Lee, and L. Magaard, 1984: Geographic and seasonal distributions of Brunt–Väisälä frequency and Rossby radii in the North Atlantic and North Pacific. *J. Phys. Oceanogr.*, **14**, 294–317.. [Find this article online](#)
- Frankignoul, C., and P. Müller, 1979: Quasi-geostrophic response of an infinite β -plane ocean to stochastic forcing by the atmosphere. *J. Phys. Oceanogr.*, **19**, 104–127.. [Find this article online](#)
- Gent, P. R., J. Willebrand, T. J. McDougall, and J. C. McWilliams, 1995: Parameterizing eddy-induced tracer transports in ocean circulation models. *J. Phys. Oceanogr.*, **25**, 463–474.. [Find this article online](#)
- Gill, A. E., 1982: *Atmosphere–Ocean Dynamics*. Academic Press, 662 pp..
- Gould, W. J., 1983: The Northeast Atlantic Ocean. *Eddies in Marine Science*, A. R. Robinson, Ed., Springer-Verlag, 145–157..
- , 1985: Physical oceanography of the Azores Front. *Progress in Oceanography*, Vol. 14, Pergamon, 167–190..
- Le Groupe Tourbillon, 1983: The Tourbillon Experiment: A study of a mesoscale eddy in the eastern North Atlantic. *Deep-Sea Res.*, **30**, 475–511..

Howe, M. R., and R. I. Tait, 1967: A subsurface cold-core cyclonic eddy. *Deep-Sea Res.*, **14**, 373–378..

Hua, B. L., 1988: The internal barotropic instability of surface-intensified eddies. Part I: Generalized theory for isolated eddies. *J. Phys. Oceanogr.*, **18**, 40–55.. [Find this article online](#)

Krauss, W., R. Döscher, A. Lehman, and T. Viehoff, 1990: On eddy scales in the eastern and northern North Atlantic Ocean as a function of latitude. *J. Geophys. Res.*, **95**, 18 049–18 056..

Kupferman, S. L., G. A. Becker, W. F. Simmons, U. Schauer, M. G. Marietta, and H. Nies, 1986: An intense cold-core eddy in the north-east Atlantic. *Nature*, **319-6**, 474–477..

Le Traon, P. Y., 1993: Comments on “Mesoscale variability in the North Atlantic Ocean from Geosat altimetry and WOCE high-resolution numerical modeling.” *J. Phys. Oceanogr.*, **23**, 2729–2732.. [Find this article online](#)

—, M. C. Rouquet, and C. Boissier, 1990: Spatial scales of mesoscale variability in the North Atlantic as deduced from GEOSAT data. *J. Geophys. Res.*, **95**, 20 267–20 285..

—, C. Boissier, and P. Gaspar, 1991: Analysis of errors due to polynomial adjustments of altimeter profiles. *J. Atmos. Oceanic Technol.*, **8**, 385–396..

McCartney, M. S., and L. D. Talley, 1982: The subpolar mode water of the North Atlantic Ocean. *J. Phys. Oceanogr.*, **12**, 1169–1188.. [Find this article online](#)

McWilliams, J. C., and G. R. Flierl, 1979: On the evolution of isolated, nonlinear vortices. *J. Phys. Oceanogr.*, **9**, 1155–1182.. [Find this article online](#)

Mercier, H., and A. Colin de Verdière, 1985: Space and time scales of mesoscale motions in the eastern North Atlantic. *J. Phys. Oceanogr.*, **15**, 171–183.. [Find this article online](#)

Müller, T. J., and G. Siedler, 1992: Multi-year current time series in the eastern North Atlantic Ocean. *J. Mar. Res.*, **50**, 63–98..

Paillet, J., and M. Arhan, 1996: Shallow pycnoclines and mode water subduction in the eastern North Atlantic. *J. Phys. Oceanogr.*, **26**, 96–114.. [Find this article online](#)

—, and H. Mercier, 1997: An inverse model of the eastern North Atlantic general circulation and thermocline ventilation. *Deep-Sea Res.*, **44**, 1293–1328..

—, M. Arhan, and M. S. McCartney, 1998: The spreading of Labrador Sea Water in the eastern North Atlantic. *J. Geophys. Res.*, **103** (C5), 10 223–10 239..

Pingree, R. D., and B. Le Cann, 1990: Structure, strength and seasonality of the slope currents in the Bay of Biscay region. *J. Mar. Biol. Assoc. U.K.*, **70**, 857–885..

—, and —, 1991: Drifting buoy in the field of flow of two eddies on east Thulean Rise (Northeast Atlantic). *J. Geophys. Res.*, **96**, 16 759–16 777..

—, and —, 1992: Three anticyclonic Slope Water oceanic eddies (SWODDIES) in the southern Bay of Biscay in 1990. *Deep-Sea Res.*, **39**, 1147–1175..

—, and —, 1993: A shallow meddy (a SMEDDY) from the secondary Mediterranean salinity maximum. *J. Geophys. Res.*, **98**, 20 169–20 185..

Pollard, R. T., M. J. Griffiths, S. A. Cunningham, J. F. Read, F. F. Perez, and A. F. Rios, 1996: Vivaldi 1997—A study of the formation, circulation and ventilation of Eastern North Atlantic central water. *Progress in Oceanography*, Vol. 37, Pergamon, 767–792..

Polvani, L. M., J. C. McWilliams, M. A. Spall, and R. Ford, 1994: The coherent structures of shallow-water turbulence: Deformation-radius effects, cyclone–anticyclone asymmetry, and gravity-wave generation. *Chaos*, **4**(2), 177–186..

Rhines, P. B., 1979: Geostrophic turbulence. *Annu. Rev. Fluid Mech.*, **11**, 401–441..

Richardson, P. L., 1983: Gulf Stream Rings. *Eddies in Marine Science*, A. R. Robinson, Ed., Springer-Verlag, 19–45..

—, M. S. McCartney, and C. Maillard, 1991: A search for meddies in historical data. *Dyn. Atmos. Oceans*, **15**, 241–265..

Schauer, U., 1989: A deep saline cyclonic eddy in the west European Basin. *Deep-Sea Res.*, **36**, 1549–1565..

Schultz Tokos, K., H. H. Hinrichsen, and W. Zenk, 1994: Merging and migration of two meddies. *J. Phys. Oceanogr.*, **24**, 2129–2141.. [Find this article online](#)

Stammer, D., and C. W. Böning, 1992: Mesoscale variability in the Atlantic Ocean from GEOSAT altimetry and WOCE high-resolution numerical modeling. *J. Phys. Oceanogr.*, **22**, 732–752.. [Find this article online](#)

—, and —, 1996: Generation and distribution of mesoscale eddies in the North Atlantic Ocean. *The Warmwatersphere of the North Atlantic Ocean*, W. Krauss, Ed., Gebrüder Borntraeger, 159–193..

—, H. H. Hinrichsen, and R. H. Käse, 1991: Can meddies be detected by satellite altimetry? *J. Geophys. Res.*, **96**, 7005–7014..

—, R. Tokmakian, A. Semtner, and C. Wunsch, 1996: How well does a $1/4^\circ$ global circulation model simulate large-scale observations? *J. Geophys. Res.*, **101** (C10), 25 779–25 811..

Stommel, H., P. Niiler, and D. Anati, 1978: Dynamic topography and recirculation of the North Atlantic. *J. Mar. Res.*, **36**, 449–468..

Sy, A., 1988: Investigation of large-scale circulation patterns in the Central North Atlantic: The North Atlantic Current, the Azores Current, and the Mediterranean water plume in the area of the Mid-Atlantic Ridge. *Deep-Sea Res.*, **35**, 383–413..

Tréguier, A.M., 1992: Kinetic energy analysis of an eddy resolving primitive equation model of the North Atlantic. *J. Geophys. Res.*, **97** (C1), 687–701..

—, and B. L. Hua, 1988: Influence of bottom topography on stratified quasi-geostrophic turbulence in the Ocean. *Geophys. Astrophys. Fluid Dyn.*, **43**, 265–305..

Tsuchiya, M., L. D. Talley, and M. S. McCartney, 1992: An Eastern Atlantic section from Iceland southward across the equator. *Deep-Sea Res.*, **39**, 1885–1917..

Tychensky, A., and X. J. Carton, 1998: Hydrological and dynamical characterization of meddies in the Azores region: A paradigm for baroclinic vortex dynamics. *J. Geophys. Res.*, in press..

—, P. Y. Le Traon, F. Hernandez, D. Jourdan, and P. Canceill, 1998: Large structures and temporal change in the Azores Front during the SEMAPHORE experiment. *J. Geophys. Res.*, in press..

Tables

Table 1. Dataset properties.

Dataset	Number of profiles	Total length	Average resolution	Average line length
XBT	2914	74 750 km	26 km	850 km
CTD	534	34 480 km	66 km	2300 km

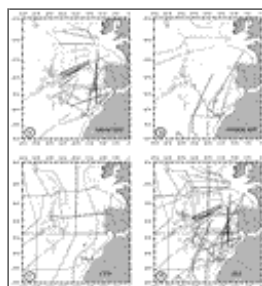
[Click on thumbnail for full-sized image.](#)

Table 2. Dynamical properties of the CW vortices detected on CTD lines, with their standard deviations.

	β_{eddy} (10^{-4})	ζ (10^{-4})	R_o	η (cm)
Cyclones	20.2 ± 10.3	9.2 ± 4.8	0.06 ± 0.04	-11.5 ± 9.3
Anticyclones	17.6 ± 8.3	-6.8 ± 3.8	0.04 ± 0.04	12.2 ± 6.0

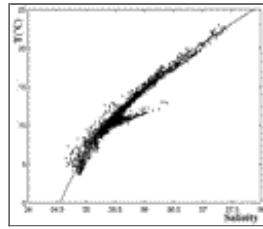
[Click on thumbnail for full-sized image.](#)

Figures



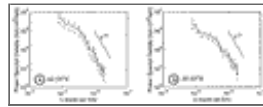
[Click on thumbnail for full-sized image.](#)

Fig. 1. Locations of hydrographic profiles: (a) SHOM XBT lines, (b) XBT lines from other sources (see text), (c) CTD lines, (d) all data. Also shown is the 2000-m isobath.



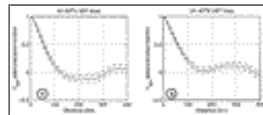
Click on thumbnail for full-sized image.

Fig. 2. Temperature–salinity relation between 100-m and 700-m depth for the CTD dataset of Fig. 1c. Solid line is the second-degree polynomial fit $\hat{S}(T)$.



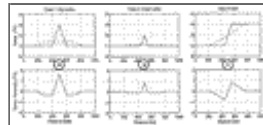
Click on thumbnail for full-sized image.

Fig. 3. Normalized 1D wavenumber spectra of H_{dyn} , averaged in (a) the 40°–55°N band and (b) the 20°–40°N band. Dashed lines represent the 95% confidence intervals.



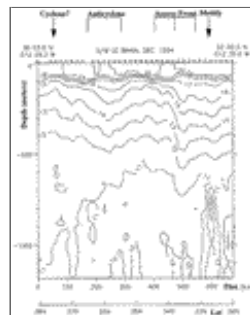
Click on thumbnail for full-sized image.

Fig. 4. Normalized autocovariance function of H_{dyn} and its statistical uncertainty, estimated from XBT lines in (a) the 40°–55°N and (b) the 20°–40°N band.



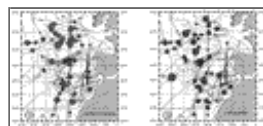
Click on thumbnail for full-sized image.

Fig. 5. Horizontal distribution of T (upper, solid), of 500-km low-passed \bar{T} (upper, dashed), and temperature anomaly ΔT (lower) at a given level for three simple cases of mesoscale perturbation: (a) large and intense vortex, (b) small vortex, (c) thermal front.



Click on thumbnail for full-sized image.

Fig. 6. Temperature section along the XBT line gathered by S/M *Le Bihan* in December 1994, along 12°30'W. Mesoscale features described in the text are noted on top of the figure.



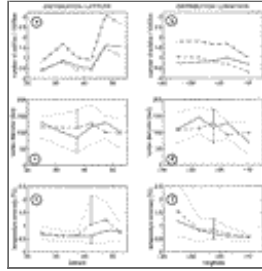
Click on thumbnail for full-sized image.

Fig. 7. Positions of (a) the selected anticyclones and (b) cyclones. Circle size is proportional to the apparent diameter of each vortex, and corresponds to the Mercator scale at 45°N.



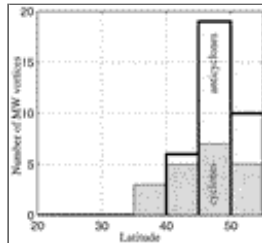
Click on thumbnail for full-sized image.

Fig. 8. Pilot chart of vortex distribution. For each geographic box the total length of hydrographic lines inside the box, the number of selected anticyclones (anti.) and cyclones (cyc.), with their average apparent diameter \bar{D}_a , the probability of vortex encounter P_V in 10^{-3} km^{-1} (or vortex per 1000 km of line), and the estimated range of coexisting vortices N_V are listed.



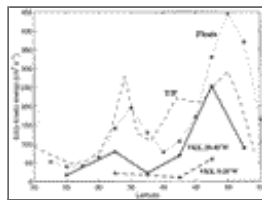
Click on thumbnail for full-sized image.

Fig. 9. Meridional (left) and zonal (right) evolutions of P_V (a, b), of \bar{D}_a (c, d), and of $|\overline{\Delta T}|$ the mean vortex temperature anomaly between 100 m and 700 m (e, f). Solid lines: anticyclones, dashed lines: cyclones, dash-dotted line: the total on (a, b). Standard deviations in (c)–(e) are shown by dotted lines on one side of each curve. Geographic averages are computed in boxes bounded by latitudes $20^\circ, 30^\circ, 35^\circ, 40^\circ, 45^\circ, 50^\circ,$ and 55°N (left plots), and by longitudes $40^\circ, 30^\circ, 25^\circ, 20^\circ, 15^\circ,$ and 5°W (right plots).



Click on thumbnail for full-sized image.

Fig. 10. Number of CW vortices containing mode water in the depth range 200–500 m, computed in 5° latitude bands. Thick lines stand for anticyclones, thin lines for cyclones.



Click on thumbnail for full-sized image.

Fig. 11. Evolution, with latitude, of the vortex kinetic energy (VKE) at 100-m depth in bands $0^\circ\text{--}20^\circ\text{W}$ (thick dashed line) and $20^\circ\text{--}40^\circ\text{W}$ (thick solid line), of the total subinertial EKE at 100 m estimated from float data along 30°W by Brüggé (1995) (dotted line and stars), and of the surface EKE estimated from TOPEX/Poseidon data smoothed on a scale of 30 km, along 30°W , by Stammer and Böning (1996) (thin dashed line).

$$^2 \hat{S} = 3.2926 \times 10^{-3} T^2 + 5.0882 \times 10^{-2} T + 34.5528.$$

³ If the horizontal sampling is regular, this filter is equivalent to a running mean over the same window.

Corresponding author address: Dr. Jérôme Paillet, EPSHOM, 13, rue du Chatellier BP426, B.P. 426, 29275 Brest Cedex, France.

E-mail: paillet@shom.fr

top ▲



© 2008 American Meteorological Society [Privacy Policy and Disclaimer](#)

Headquarters: 45 Beacon Street Boston, MA 02108-3693

DC Office: 1120 G Street, NW, Suite 800 Washington DC, 20005-3826

amsinfo@ametsoc.org Phone: 617-227-2425 Fax: 617-742-8718

[Allen Press, Inc.](#) assists in the online publication of *AMS* journals.